

1 This document is the author’s post-print version of this article,
2 i.e. the final draft version after review. The final document is
3 printed in *Nuclear Instruments and Methods in Physics Research*
4 *Section A: Accelerators, Spectrometers, Detectors and Associated*
5 *Equipment* **735**, p. 644-648 (2014) and can be viewed online by us-
6 ing the DOI 10.1016/j.nima.2013.10.044. We also refer to this URL
7 for full bibliographic details.

High spectral and spatial resolution X-ray transmission radiography and tomography using a Color X-ray Camera

Matthieu N. Boone^a, Jan Garrevoet^b, Pieter Tack^b, Oliver Scharf^c, David P. Cormode^d, Denis Van Loo^a, Elin Pauwels^a, Manuel Dierick^a, Laszlo Vincze^b, Luc Van Hoorebeke^a

^a*Ghent University, Dept. Physics and Astronomy
Proeftuinstraat 86; B-9000 Gent, Belgium*

^b*Ghent University, Dept. Analytical Chemistry
Krijgslaan 281/S12; B-9000 Gent, Belgium*

^c*IfG-Institute for Scientific Instruments GmbH
Rudower Chaussee 29/31; D-12489 Berlin, Germany*

^d*University of Pennsylvania, Depts. Radiology, Cardiology and Bioengineering
O3400 Spruce St, 1 Silverstein; Philadelphia, PA 19104, USA*

Abstract

High resolution X-ray radiography and computed tomography are excellent techniques for non-destructive characterization of an object under investigation at a spatial resolution in the micrometer range. However, as the image contrast depends on both chemical composition and material density, no chemical information is obtained from this data. Furthermore, lab-based measurements are affected by the polychromatic X-ray beam, which results in beam hardening effects. New types of X-ray detectors which provide spectral information on the measured X-ray beam can help to overcome these limitations. In this paper, an energy dispersive CCD detector with high spectral resolution is characterized for use in high resolution radiography and tomography, where a focus is put on the experimental conditions and requirements of both measurement techniques.

Keywords: Computed tomography, Color X-ray Camera, pnCCD, Spectral X-ray imaging

PACS: 07.85.Nc, 87.59.-e, 07.57.Kp

1. Introduction

High resolution X-ray radiography and computed tomography are excellent techniques for non-destructive investigation of small objects. Standard

laboratory-based setups allow for a 2D or 3D visualization at a spatial resolution level in the micrometer range, hence giving very useful information on the internal microstructure of the object. However, the image contrast is based on the linear attenuation coefficient of the object material, which depends on both the material composition and density. Chemical information is thus not directly available in standard radiography and tomography. Furthermore, the continuous X-ray spectrum used in laboratory-based setups combined with the energy dependent linear attenuation coefficient results in beam hardening effects. Although synchrotron-based setups allow for quasi-monochromatic radiation, they have limited accessibility.

These limitations can be partly overcome by the use of a new type of pixelated X-ray detectors, which provide spectral information on the measured X-ray beam. This is achieved by measuring the deposited energy of each photon separately and classifying each measured photon or event based on this information. These devices can be roughly divided into two categories. A first category comprises the so-called single photon counting or multispectral detectors, which count every incident photon separately by analyzing instantaneously the electrical pulse associated with the deposited energy in a single pixel and comparing this with one or more reference energies. As such, one or several energy thresholds can be achieved. Despite the limited number of energy bins, several results illustrating the advantages for material identification have been published using a variety of detectors [1, 2, 3, 4, 5, 6, 7, 8, 9]. A second category comprises the so-called hyperspectral detectors, which measure the energy deposited in each pixel during a certain exposure time and consequently reconstruct the associated photon energy and discretize the spectrum. The detector readout and analysis however reduce the available measurement speed and count rate. These devices are typically based on direct detection in a CCD system [10, 11], yet a hybrid system using a CdTe sensor bump-bonded to a readout ASIC has been presented as well, which allows for higher X-ray energies to be detected [12, 13].

In this paper, we present the characteristics of a CCD-based hyperspectral detector as a detector system for X-ray radiography and high resolution tomography. We present an example of chemical identification based on a single radiograph and the count rate limitations which are imposed by the operation of the detector and the incident spectrum. To conclude, we present the results of a spectral high resolution CT scan using this detector.

2. Materials and methods

2.1. Color X-ray Camera

The hyperspectral detector used in this work is the Color X-ray Camera or SLcam [14, 15]. The center stage of this device is taken by the pnCCD detector chip. This chip, designed for ultrafast readout, was originally developed as a spectroscopic X-ray imager for the astrophysical satellite mission XMM-Newton

[16, 17]. It has since been adapted to be used in many other applications such as high energy electron imaging, energy-resolved two-dimensional X-ray diffraction and scattering experiments at synchrotron facilities [14].

In the case of the SLcam, a pnCCD chip of 528×264 pixels of $48^2 \mu\text{m}^2$ is used, of which only the central 264×264 pixels are used as X-ray detector. At each side, an area of 132×264 pixels is used as storage region. Each half image is transferred to the X-ray shielded storage region within $50 \mu\text{s}$, reducing the effect of illumination during charge transfer [14]. The charges in the storage region are subsequently amplified, read out by a multi-channel readout ASIC for additional signal amplification, filtering and multiplexing and transferred to a separate data acquisition system and digitizer at a frame rate of 400 Hz. The digitized frames are transmitted to a high-performance measurement computer where they are further processed by the readout software.

Due to the relatively small pixel size and large depletion depth of $450 \mu\text{m}$, the charge cloud created by the incident photon will often not be limited to single a pixel, hence creating an *event cluster*. To successfully reconstruct the deposited energy and the position of each photon separately, an event analysis is performed on each frame and the total deposited energy and center of gravity of each event cluster is calculated. This method yields a spatial resolution very close to the sampling limit [14]. At the operating temperature of approximately -20°C , the resulting spectral resolution is approximately 150 eV FWHM at Mn $K\alpha$, which is comparable to state-of-the-art single-element energy-dispersive detectors. The imaging system is thus very attractive for full-field X-ray fluorescence imaging (XRF) [15, 18, 19] or X-ray absorption near edge spectroscopy [20] and has previously been characterized for this purpose. In this paper, the SLcam will however be characterized for usage with transmission X-ray radiography and computed tomography. Due to the low detection efficiency of the Si sensor at higher photon energies, these measurements are limited to a low-energy spectrum below 25 keV. Consequently, only samples with a limited thickness or limited size can be measured.

2.2. Measurement setup

The measurements have been performed at the Ghent University Center for X-ray Tomography (UGCT) micro-CT setup [21]. The X-ray tube is a dual-head system from FeinFocus, of which the FXE160.51 transmission head has been used for this work. A tungsten target with a thickness of $5 \mu\text{m}$ and a molybdenum target with a thickness of $1 \mu\text{m}$ have been used. In the spectrum of the former, a large number of characteristic lines from W are present, as well as two characteristic lines of Mo originating from the secondary radiation in the X-ray tube head [22]. In the spectrum of the Mo target, only the characteristic lines of molybdenum are present. All measurements have been performed at an accelerating voltage of 40 kV. The samples were mounted on a motorized stage to allow for accurate positioning. The source-to-detector distance amounts to approximately 900 mm to ensure a stable operation of the X-ray tube at very low

117 flux at the detector side. Additionally, this allows for a large source-to-object
 118 distance to reduce the heat load on the sample during the long measurement
 119 times.

120 **3. Results and discussion**

121 *3.1. Spectral absorption radiography*

In spectral absorption radiography, the energy dependency of the linear attenuation coefficient of the object under investigation can be measured. More particularly, absorption edges can be observed and used to identify the chemical composition of an object. These edges can best be visualized using the projected attenuation coefficient $\mu_\theta(x, y, E)$:

$$\mu_\theta(x, y, E) = \int_{\text{raypath}} \mu(x', y', z', E) ds(x', y', z'), \quad (1)$$

where (x, y) and (x', y', z') are the detector and object coordinate systems, respectively, E is the photon energy, μ is the linear attenuation coefficient and θ denotes the projection angle in tomography. This value can easily be derived from the normalized projection images:

$$\mu_\theta(x, y, E) = -\ln \left[\frac{I_\theta(x, y, E)}{I_0(x, y, E)} \right], \quad (2)$$

122 where $I_\theta(x, y, E)$ and $I_0(x, y, E)$ are the measured intensity with and without the
 123 object, respectively. As the intensity is measured for each energy bin separately,
 124 the projected attenuation can be plotted as a function of photon energy for each
 125 pixel individually or for a region of interest. This is illustrated in Figure 1,
 126 where the projected attenuation coefficient of a tungsten transmission target
 127 (nominal thickness 5 μm on a carbon backing of 250 μm thickness) is shown and
 128 compared with the theoretically expected value. The latter has been obtained
 129 by calculating the photoelectric absorption of the attenuated beam in a 450 μm
 130 thick Si slab. The attenuated beam spectrum was calculated using Monte Carlo
 131 simulations of the X-ray tube [22] and the attenuation coefficients of W and C
 132 from the NIST database. The W L-edges are clearly visible on the curve. Below
 133 7 keV, the curve is distorted due to the very low X-ray transmission through
 134 the object and Compton scattering in the detector, whereas above 17 keV the
 135 characteristic radiation in the incident spectrum from the molybdenum target
 136 and pulse pileup effects severely influence the curve.

137 *3.2. Pulse pileup*

138 Contrary to multispectral devices, pulse pileup in the SLcam is not caused
 139 by a temporal overlap of two pulses within one pixel, but rather by a spatial
 140 overlap of two events within one readout cycle (i.e. 2.5 ms). This results in a
 141 fundamentally different manifestation of the effect. Indeed, when such spatial
 142 overlap occurs and the event is considered valid (i.e. the cluster did not become

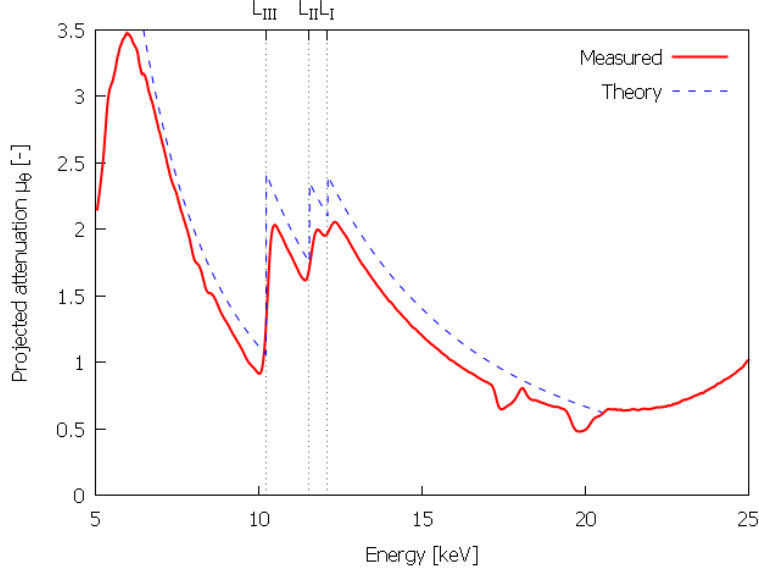


Figure 1: The projected attenuation μ_θ of a tungsten transmission target. The absorption edges of W are indicated. The structures between 17 keV and 20 keV are caused by the incident spectrum.

too large), the reconstructed photon energy will equal the sum of both photon energies. In multispectral devices the pulse height, hence the measured photon energy, depends largely on the temporal overlap and shape of both pulses [23]. In XRF applications, this behavior is desired as it results in distinct sum peaks rather than a continuous spectrum. In absorption radiography on the other hand, the behavior is less predictable, but it can give rise to a clear deduplication of the absorption edge at energy levels corresponding with the multiples of the absorption edge energy. This is shown in Figure 2, which shows the projected attenuation of a copper mesh along with the linear attenuation coefficient of Cu. Besides the absorption edge at 8.993 keV, a deduplication at approximately 18 keV is observed. It should be noted that the flatfield exposure time was lower than the image exposure time due to a failure of the X-ray tube, hence the negative values of the attenuation coefficient. As such, both vertical axes are not directly related. An absorption edge is clearly visible at the energy corresponding to twice the energy of the absorption edge of Cu. It should be noted that this measurement is performed using the W target, of which the characteristic radiation is positioned near the absorption edge of Cu. This explains the various peaks in the absorption edge and its deduplicated version.

3.3. Fluorescent radiation

In Figure 2, a substantial amount of features in the range from 5 keV to 8 keV can be observed. These can be associated with peaks in the flat-field spectrum

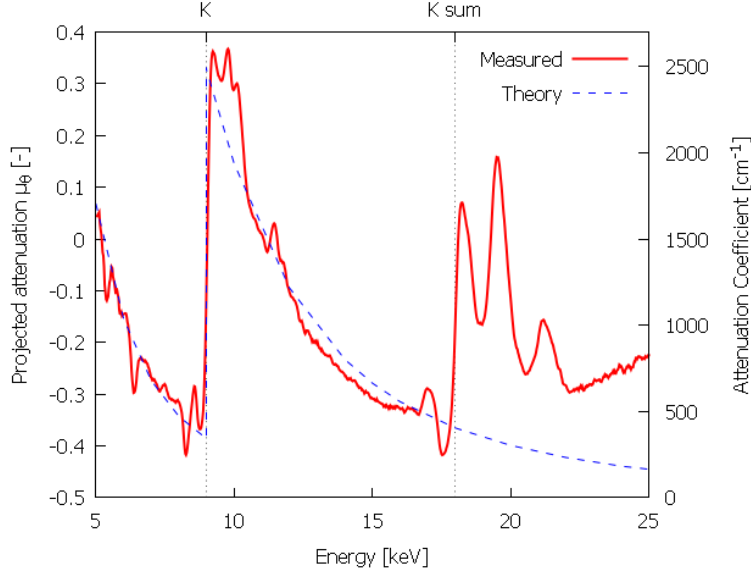


Figure 2: The projected attenuation μ_0 of a copper mesh. The absorption edge of Cu at 9 keV as well as its double at 18 keV are indicated. A substantial effect from the characteristic radiation in the incident spectrum is observed. The negative attenuation coefficients are due to a reduced exposure time of the flatfield image.

164 originating from fluorescent radiation from metals near the sensor. A similar
 165 effect has been reported in other systems, with fluorescent radiation originating
 166 from the chipboard [24] or from the sensor material itself [9].

167 3.4. Count rate limitation

168 A major limitation in the practical application of the SLcam is imposed by
 169 the allowed count rates of the detector. Indeed, when the incident X-ray flux is
 170 too large, the event clusters will overlap and get rejected by the analysis soft-
 171 ware. This is a statistical process, hence the limit is not strictly defined but is
 172 rather a deviation from ideal behavior as a function of the count rate. This is
 173 shown in Figure 3, where the measured count rate is plotted as a function of
 174 the deposited energy in the chip. The latter is calculated before processing of
 175 the frames and is proven to be linearly dependent with intercept zero on the
 176 X-ray flux. The curve shows a deviation from a linear response and even starts
 177 to decrease as the X-ray flux is further increased.

178
 179 Furthermore, it is observed that the response curve depends on the inci-
 180 dent spectrum which was varied based on the target material (W or Mo) and
 181 on an additional beam filter (100 μm Al). As the object under investigation
 182 influences the X-ray spectrum due to beam hardening, the X-ray flux should
 183 be kept sufficiently low to minimize the deviation from a linear response. This
 184 is particularly the case in the presence of characteristic radiation, which may

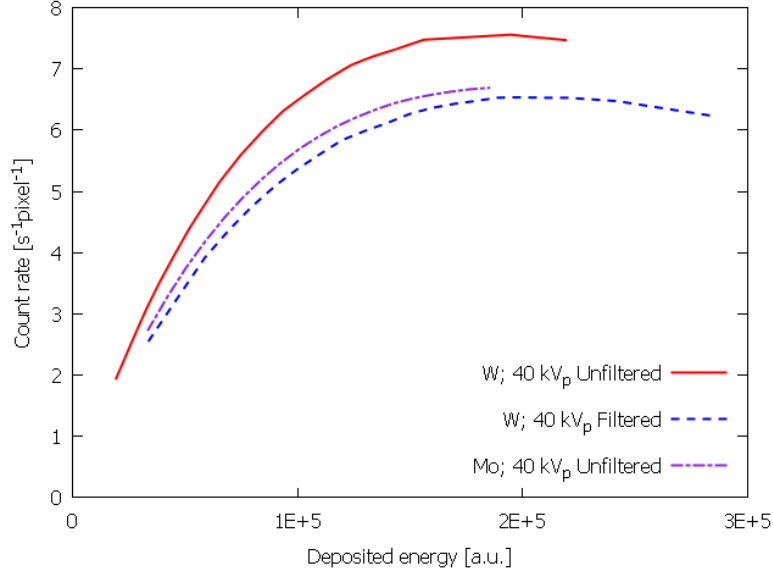


Figure 3: The measured count rate (per pixel) as a function of the total deposited energy for three different X-ray spectra using two different target materials and different beam filtering.

dominate the X-ray spectrum. This is the case in Figure 2 and is manifested by the fine structure of the curve.

A reduction of the X-ray flux however results in lower signal-to-noise ratio (SNR). From Figure 3, it is evident that the measured count rate will be less than 8 s^{-1} per pixel. This leads to measurement times of several minutes per image for X-ray radiography and tomography. Additionally, a large portion of the detected counts are associated with characteristic radiation, further reducing the number of counts at energy ranges away from this characteristic radiation. The use of target materials with a limited characteristic radiation yield in the considered spectral range is therefore expected to substantially improve the performance of the SLcam in transmission radiography.

3.5. Computed tomography

Using the SLcam, a full spectral high resolution CT dataset has been acquired. The object under investigation is an aortic arch taken from a mouse model of atherosclerosis. The mouse had been injected with gold high-density lipoprotein nanoparticle contrast agent (Au-HDL) before sacrifice, which accumulates in the atherosclerotic plaque in the artery. [25, 26]. The sample thus consists of low-density material (the artery itself) with high-density inclusions which can be either calcifications or gold nanoparticles. It is however impossible to separate and identify both phases in conventional micro-CT. Using 2D

micro-XRF Ca, Au and Zn have been observed in the sample, as well as a small concentration of Cu. Due to the complex geometry of the sample (Figure ??), these results could not be linked to the conventional micro-CT scan. A spectral micro-CT scan has thus been acquired to provide this information.

The spectral CT scan consists of 180 equi-angular projections covering 360°. Each projection consists of 1024 energy bins with an energy bin size of approximately 25 eV and has been recorded with an exposure time of 20 mins. To reduce image noise, a limited number of spectral regions has been selected. This is summarized in Table 1 where absorption edges and the average number of counts (per pixel) in the unattenuated beam are indicated. It should be noted that the SNR can be deduced directly from the latter following Poisson statistics. The attenuation coefficient of Ca, Zn and Au are plotted in Figure 4, on which the spectral regions are indicated.

Region	Start energy	End energy	Edges	Counts
R0	6.75 keV	8.25 keV	—	305
R1	8.25 keV	9.50 keV	Cu K	412
R2	9.50 keV	11.00 keV	Zn K	573
R3	11.00 keV	12.50 keV	Au L3	552
R4	12.50 keV	15.00 keV	Au L2,1	737
R5	15.00 keV	17.00 keV	—	424

Table 1: The spectral regions used in the analysis of the tomographic dataset of the artery sample. For each region, start energy and end energy are given along with the absorption edges present in the region and the mean number of flat-field counts per pixel.

As expected, the reconstructed attenuation coefficient decreases for increasing photon energy for all materials, and this effect is stronger in the calcified regions than in the soft tissue. One such result is visualized in Figure ??, where the difference between regions R5 and R4 is rendered in 3D. No spectral features are expected in this differential dataset. Only noise is indeed visible in these reconstructed slices and the 3D rendering, which shows only the positive values. Crossing an absorption edge however, the attenuation coefficient locally increases for increasing energy. This is visualized in Figure ??, where the difference between regions R4 and R2 is rendered. Some strongly positive *hot spots* are clearly visible in the sample, indicating an increase in attenuation coefficient hence the presence of gold.

The presented results should however be interpreted with care. The voxel size of the reconstructed volume is approximately $16^3 \mu\text{m}^3$, which is insufficient to image the fine-structured calcification and partial volume effects are significant. A particular problem is raised by the different behavior of the attenuation coefficients of Ca and Au around the Au absorption edges. Indeed, the effect of the Au absorption edge might be cancelled out by the strongly decreasing

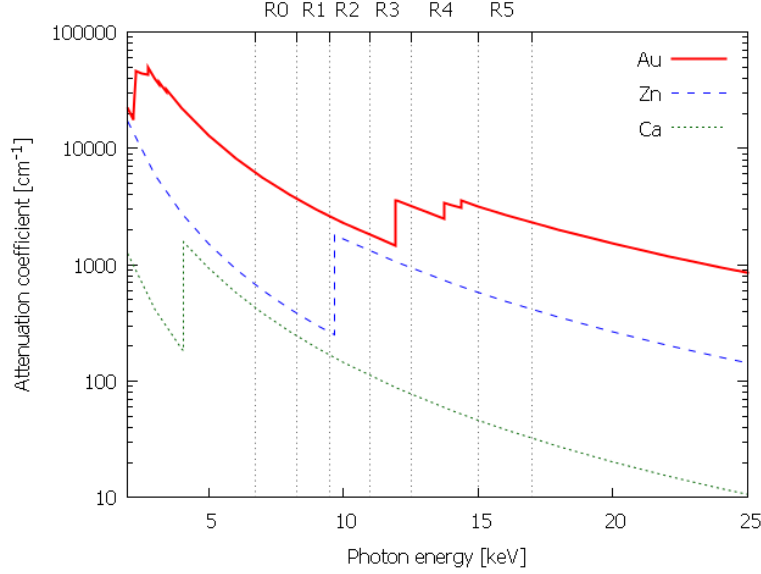


Figure 4: The attenuation coefficient of Ca, Zn and Au for the photon energies measured by the SLcam. The spectral regions (Table 1) are indicated on the graph.

attenuation coefficient of Ca within that voxel (Figure 4). Furthermore, the low SNR of the datasets should be kept in mind.

4. Conclusion

The use of energy-dispersive 2D detectors in high resolution X-ray radiography and tomography can yield chemical information and structural information simultaneously. However, several challenges still remain. Most importantly, the reduction of the incident X-ray flux, required for the single photon counting mechanisms, implies an important increase in image noise and measurement time. This effect becomes even more important when only a (small) energy bin is considered to exploit the spectral data. Secondly, the sensor material implies specific limitations. Silicon sensors such as the pnCCD have a limited detection efficiency at photon energies above 20 keV and hence can only be used for small samples or samples with limited X-ray attenuation. Highly attenuating sensor materials such as Cd(Zn)Te on the other hand are frequently used in hybrid detector systems for spectroscopic imaging (e.g. [12, 9]) but typically contain a large amount of crystal defects and suffer from X-ray fluorescence inside the sensor material.

Despite these limitations, as detector technology is developing swiftly, energy-dispersive radiography and tomography is becoming an increasingly studied research topic.

5. Acknowledgements

The authors gratefully acknowledge IWT-Flanders for the doctoral grant of Jan Garrevoet and Pieter Tack. David P. Cormode is supported by NIH grant R00 EB012165. The Special Research Fund of the Ghent University (BOF) is acknowledged for the financial support (GOA 01G01008).

- [1] B. Norlin, A. Manuilskiy, H. E. Nilsson, C. Frodh, Material recognition with the Medipix photon counting colour X-ray system, *Nucl. Instrum. Methods Phys. Res., Sect. A* 531 (1-2) (2004) 265–269.
- [2] A. P. H. Butler, N. G. Anderson, R. Tipples, N. Cook, R. Watts, J. Meyer, A. J. Bell, T. R. Melzer, P. H. Butler, Bio-medical X-ray imaging with spectroscopic pixel detectors, *Nucl. Instrum. Methods Phys. Res., Sect. A* 591 (1) (2008) 141–146.
- [3] M. Firsching, P. T. Talla, T. Michel, G. Anton, Material resolving X-ray imaging using spectrum reconstruction with Medipix2, *Nucl. Instrum. Methods Phys. Res., Sect. A* 591 (1) (2008) 19–23.
- [4] J. P. Schlomka, E. Roessl, R. Dorscheid, S. Dill, G. Martens, T. Istel, C. Baumer, C. Herrmann, R. Steadman, G. Zeitler, A. Livne, R. Proksa, Experimental feasibility of multi-energy photon-counting K-edge imaging in pre-clinical computed tomography, *Phys. Med. Biol.* 53 (15) (2008) 4031–4047.
- [5] M. Firsching, A. P. Butler, N. Scott, N. G. Anderson, T. Michel, G. Anton, Contrast agent recognition in small animal CT using the Medipix2 detector, *Nucl. Instrum. Methods Phys. Res., Sect. A* 607 (1) (2009) 179–182.
- [6] P. M. Shikhaliev, S. G. Fritz, Photon counting spectral CT versus conventional CT: comparative evaluation for breast imaging application, *Phys. Med. Biol.* 56 (7) (2011) 1905–1930.
- [7] J. Uher, J. Jakubek, Equalization of Medipix2 imaging detector energy thresholds using measurement of polychromatic X-ray beam attenuation, *J. Instr.* 6 (2011) C11012.
- [8] X. Wang, D. Meier, S. Mikkelsen, G. E. Maehlum, D. J. Wagenaar, B. M. W. Tsui, B. E. Patt, E. C. Frey, MicroCT with energy-resolved photon-counting detectors, *Phys. Med. Biol.* 56 (9) (2011) 2791–2816.
- [9] T. Koenig, J. Schulze, M. Zuber, K. Rink, J. Butzer, E. Hamann, A. Cacilia, A. Zwerger, A. Fauler, M. Fiederle, U. Oelfke, Imaging properties of small-pixel spectroscopic x-ray detectors based on cadmium telluride sensors, *Phys. Med. Biol.* 57 (2012) 6743–6759.
- [10] H. Tsunemi, S. Kawai, K. Hayashida, PERFORMANCE OF THE CHARGE-COUPLED DEVICE FOR DIRECT X-RAY-DETECTION IN THE ENERGY-RANGE OF 1-9 KEV AT THE SYNCHROTRON RADIATION FACILITY, *Jpn. J. Appl. Phys., Part 1* 30 (6) (1991) 1299–1302.

- [11] N. Meidinger, R. Andritschke, O. Haelker, R. Hartmann, S. Herrmann, P. Holl, G. Lutz, N. Kimmel, G. Schaller, M. Schnecke, F. Schopper, H. Soltau, L. Struder, Next generation of pnCCDs for X-ray spectroscopy and imaging, Nucl. Instrum. Methods Phys. Res., Sect. A 568 (1) (2006) 141–148.
- [12] P. Seller, S. Bell, R. J. Cernik, C. Christodoulou, C. K. Egan, J. A. Gaskin, S. Jacques, S. Pani, B. D. Ramsey, C. Reid, P. J. Sellin, J. W. Scuffham, R. D. Speller, M. D. Wilson, M. C. Veale, Pixellated Cd(Zn)Te high-energy X-ray instrument, J. Instr. 6 (2011) C12009.
- [13] M. D. Wilson, S. J. Bell, R. J. Cernik, C. Christodoulou, C. K. Egan, D. O’Flynn, S. Jacques, S. Pani, J. Scuffham, P. Seller, P. J. Sellin, R. Speller, M. C. Veale, Multiple Module Pixellated CdTe Spectroscopic X-Ray Detector, IEEE Trans. Nucl. Sci. 60 (2) (2013) 1197–1200.
- [14] I. Ordavo, S. Ihle, V. Arkadiev, O. Scharf, H. Soltau, A. Bjeoumikhov, S. Bjeoumikhova, G. Buzanich, R. Gubzhokov, A. Gunther, R. Hartmann, P. Holl, N. Kimmel, M. Kuhbacher, M. Lang, N. Langhoff, A. Liebel, M. Radtke, U. Reinholz, H. Riesemeier, G. Schaller, F. Schopper, L. Struder, C. Thamm, R. Wedell, A new pnCCD-based color X-ray camera for fast spatial and energy-resolved measurements, Nucl. Instrum. Methods Phys. Res., Sect. A 654 (1) (2011) 250–257.
- [15] O. Scharf, S. Ihle, I. Ordavo, V. Arkadiev, A. Bjeoumikhov, S. Bjeoumikhova, G. Buzanich, R. Gubzhokov, A. Gunther, R. Hartmann, M. Kuhbacher, M. Lang, N. Langhoff, A. Liebel, M. Radtke, U. Reinholz, H. Riesemeier, H. Soltau, L. Struder, A. F. Thunemann, R. Wedell, Compact pnCCD-Based X-ray Camera with High Spatial and Energy Resolution: A Color X-ray Camera, Anal. Chem. 83 (7) (2011) 2532–2538.
- [16] L. Struder, H. Brauninger, U. Briel, R. Hartmann, G. Hartner, D. Hauff, N. Krause, B. Maier, N. Meidinger, E. Pfeffermann, M. Popp, C. Reppin, R. Richter, D. Stotter, J. Trumper, U. Weber, P. Holl, J. Kemmer, H. Soltau, A. Viehl, C. von Zanthier, A 36 cm(2) large monolithic pn-charge coupled device x-ray detector for the European XMM satellite mission, Rev. Sci. Instrum. 68 (11) (1997) 4271–4274.
- [17] L. Struder, U. Briel, K. Dennerl, R. Hartmann, E. Kendziorra, N. Meidinger, E. Pfeffermann, C. Reppin, B. Aschenbach, W. Bornemann, H. Brauninger, W. Burkert, M. Elender, M. Freyberg, F. Haberl, G. Hartner, F. Heuschmann, H. Hippmann, E. Kastelic, S. Kemmer, G. Kettenring, W. Kink, N. Krause, S. Muller, A. Oppitz, W. Pietsch, M. Popp, P. Predehl, A. Read, K. H. Stephan, D. Stotter, J. Trumper, P. Holl, J. Kemmer, H. Soltau, R. Stotter, U. Weber, U. Weichert, C. v. Zanthier, D. Carathanassis, G. Lutz, R. H. Richter, P. Solc, H. Bottcher, M. Kuster, R. Staubert, A. Abbey, A. Holland, M. Turner, M. Balasini, G. F. Bignami, N. L. Palombara, G. Villa, W. Buttler, F. Gianini, R. Laine, D. Lumb,

- 342 P. Dhez, The European Photon Imaging Camera on XMM-Newton: The
343 pn-CCD camera, *Astron. Astrophys.* 365 (1) (2001) L18–L26.
- 344 [18] G. Buzanich, M. Radtke, U. Reinholz, H. Riesemeier, A. F. Thunemann,
345 C. Streli, Impurities in multicrystalline silicon wafers for solar cells detected
346 by synchrotron micro-beam X-ray fluorescence analysis, *J. Anal. At. Spec-*
347 *trom.* 27 (11) (2012) 1875–1881.
- 348 [19] I. Reiche, K. Muller, M. Alberic, O. Scharf, A. Waehning, A. Bjeoumikhov,
349 M. Radtke, R. Simon, Discovering Vanished Paints and Naturally Formed
350 Gold Nanoparticles on 2800 Years Old Phoenician Ivories Using SR-FF-
351 MicroXRF with the Color X-ray Camera, *Anal. Chem.* 85 (12) (2013) 5857–
352 5866.
- 353 [20] Z. Savoly, G. Pepponi, P. I. Nagy, C. Streli, G. Buzanich, E. Chinea-Cano,
354 G. Zaray, Investigation of distribution and oxidation state of copper in soil-
355 inhabiting nematodes by means of synchrotron radiation, *X-Ray Spectrom.*
356 42 (4) (2013) 321–329.
- 357 [21] B. Masschaele, V. Cnudde, M. Dierick, P. Jacobs, L. Van Hoorebeke,
358 J. Vlassenbroeck, UGCT: New x-ray radiography and tomography facil-
359 ity, *Nucl. Instrum. Methods Phys. Res., Sect. A* 580 (1) (2007) 266–269.
- 360 [22] M. N. Boone, J. Vlassenbroeck, S. Peetermans, D. Van Loo, M. Dierick,
361 L. Van Hoorebeke, Secondary radiation in transmission-type X-ray tubes:
362 simulation, practical issues and solution in the context of X-ray micro-
363 tomography, *Nucl. Instrum. Methods Phys. Res., Sect. A* 661 (1) (2012)
364 7–12.
- 365 [23] X. Cheng, M. Persson, C. Han, S. Karlsson, M. Danielsson, C. Svens-
366 son, H. Bornefalk, Evaluation of a Second-Generation Ultra-Fast Energy-
367 Resolved ASIC for Photon-Counting Spectral CT, *IEEE Trans. Nucl. Sci.*
368 60 (1) (2013) 437–445.
- 369 [24] T. Michel, P. T. Talla, M. Firsching, J. Durst, M. Bohnel, G. Anton, Re-
370 construction of X-ray spectra with the energy sensitive photon counting
371 detector Medipix2, *Nucl. Instrum. Methods Phys. Res., Sect. A* 598 (2)
372 (2009) 510–514.
- 373 [25] D. P. Cormode, T. Skajaa, M. M. van Schooneveld, R. Koole, P. Jarzyna,
374 M. E. Lobatto, C. Calcagno, A. Barazza, R. E. Gordon, P. Zanzonico,
375 E. A. Fisher, Z. A. Fayad, W. J. M. Mulder, Nanocrystal Core High-Density
376 Lipoproteins: A Multimodality Contrast Agent Platform, *Nano Lett.* 8 (11)
377 (2008) 3715–3723.
- 378 [26] D. P. Cormode, E. Roessl, A. Thran, T. Skajaa, R. E. Gordon, J. P.
379 Schlomka, V. Fuster, E. A. Fisher, W. J. M. Mulder, R. Proksa, Z. A.
380 Fayad, Atherosclerotic Plaque Composition: Analysis with Multicolor CT
381 and Targeted Gold Nanoparticles, *Radiology* 256 (3) (2010) 774–782.